J. Fluid Mech. (2008), *vol.* 595, *pp.* 203–219. © 2008 Cambridge University Press
doi:10.1017/S0022112007009135 Printed in the United Kingdom

A comparison of turbulent thermal convection between conditions of constant temperature and constant heat flux

R. VERZICCO[1] AND K. R. SREENIVASAN[2]

[1]Politecnico di Bari, DIMeG and CEMeC, Via Re David 200, 70125, Bari, Italia

[2]International Centre for Theoretical Physics, Strada Costiera 11, 34014 Trieste, Italy

(Received 14 August 2006 and in revised form 14 September 2007)

We numerically investigate turbulent thermal convection driven by a horizontal surface of constant heat flux and compare the results with those of constant temperature. Below $Ra \approx 10^9$, where Ra is the Rayleigh number, when the flow is smooth and regular, the heat transport in the two cases is essentially the same. For $Ra > 10^9$ the heat transport for imposed heat flux is smaller than that for constant temperature, and is close to experimental data. We provide a simple dimensional argument to indicate that the unsteady emission of thermal plumes renders typical experimental conditions closer to the constant heat flux case.

1. Introduction

Numerical simulations of turbulent thermal convection have been performed recently by Amati *et al.* (2005) over eight decades of the Rayleigh number $2 \times 10^6 < Ra < 2 \times 10^{14}$. These simulations have allowed the determination of the non-dimensional heat transport, or the Nusselt number, Nu, for thermal convection under ideal conditions of constant Prandtl number, zero sidewall conduction, infinite thermal conductivity and heat capacity of horizontal plates, and the unconditional validity of the Boussinesq approximation. The results from the simulations differ from existing experimental data (Niemela *et al.* 2000; Chavanne *et al.* 2001). These differences can be as high as 20% (figure 1*a*). Although differences of that order, or even larger, exist between experiments performed under nominally identical conditions, it is important to understand whether there is a fundamental reason why the numerical simulations and experiments disagree. Resolving this issue is our purpose here.

Since both numerical and experimental flows were confined within a cylindrical cell of diameter to height ratio $\Gamma = 1/2$, neither the aspect ratio nor the shape of the cell could play any role in explaining the difference. It is also thought that the difference cannot be attributed to inadequate numerical resolution; some details of grid resolution have already been discussed in Verzicco & Camussi (2003) and Amati *et al.* (2005), and more systematic checks described and discussed in § 2.1 confirm this conclusion.

There are, however, several possible candidates that could contribute to the observed difference. In helium experiments, the Prandtl number did not remain constant as the operating regime of Ra was extended by approaching the thermodynamic critical point (see figure 1*b*). In the simulations, as already noted, the Prandtl number was held strictly constant. This could be a major reason for the discrepancy. Indeed, Stringano & Verzicco (2005) have recently shown that different combinations of Ra

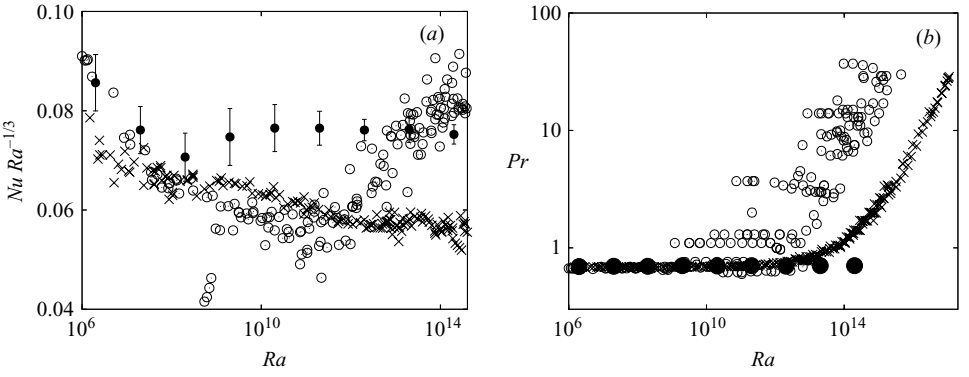

FIGURE 1. (*a*) Compensated Nusselt number versus Rayleigh number. Numerical simulations: ●, Amati *et al.* (2005). Experimental data: ○, Chavanne *et al.* (2001); ×, Niemela *et al.* (2000). (*b*) The *Ra*–*Pr* data for the different flows shown in (*a*).

and *Pr* might correspond to different mean flow structures in the same cell (see also Niemela & Sreenivasan 2003). Nevertheless, the simulations of Stringano & Verzicco (2005) have shown that this structural feature does not alter the heat transport. Experiments (Ahlers & Xu 2001; Roche *et al.* 2002; Xia, Lam & Xu 2002) show that the Prandtl number does not affect the heat transport significantly, consistent with the theoretical premise of some studies since Malkus (1954) and more recently Grossman & Lohse (2001) that the *Pr* effects are negligible when *Pr* is somewhat larger than unity (although the papers by Castaing *et al.* (1989) and Shraiman & Siggia (1990) conclude that a dependence on the Prandtl number is possible). In addition, in the helium experiments of figure 1, the Prandtl number remains essentially constant up to $Ra \approx 10^{11}$ while the differences in *Nu* appear for lower *Ra*, thus allowing us to conclude that the mismatch highlighted in figure 1 cannot be attributed to varying *Pr* in the experiments.

Another cause of concern in experiments is the violation at high values of *Ra* of the Boussinesq approximation. This feature can indeed alter the heat transport quite significantly (Niemela & Sreenivasan 2003; Ahlers *et al.* 2007), but the alteration becomes important in experiments only towards very high *Ra*. On the other hand, as shown in figure 1, the differences between numerical simulations and experiments are evident even when non-Boussinesq effects in experiments are insignificant. We thus rule out non-Boussinesq effects as the proper explanation for the differences under present consideration.

In experiments, because of the necessity to join highly conducting horizontal plates with poorly conducting sidewalls, there is a certain amount of heat leak from the sidewall to the fluid near the hot plate and a reverse heat flow from the fluid to the sidewall near the cold plate. This feature of sidewall conduction is too complex to model precisely but several models exist (Ahlers 2001; Roche *et al.* 2001; Verzicco 2002; Niemela & Sreenivasan 2003). No such corrections can account for the observed differences. For example, Niemela & Sreenivasan (2006) show that the data with and without corrections are not different enough to explain the present discrepancy. In any case, this correction is asymptotically negligible for increasing *Ra*.

The final issue is the finite conductivity of the horizontal plates. The notion that even the very large thermal conductivity of the plates could interfere with the heat transport was initially put forward by Chaumat, Castaing & Chilla (2002), later extended by Chillá *et al.* (2004). Verzicco (2004) was able to quantify this effect

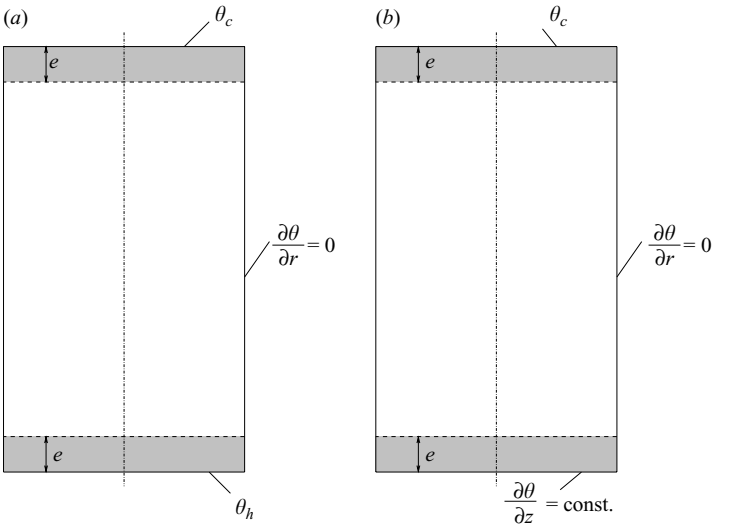

FIGURE 2. Setups with different temperature boundary conditions: (*a*) plates with constant temperature on dry surfaces, and (*b*) lower plate with constant heat flux.

and find a correction numerically. An experimental confirmation of this model was presented by Brown *et al.* (2005).

Verzicco's (2004) correction considered the limit in which the plate thickness goes to zero (or the so-called Biot number vanishes), thus ensuring, for the case of steady heat transport, that the plate remains at uniform temperature quite accurately. When the resulting plate correction is applied to measurements, the Nusselt number obtained corresponds to the absence of the thermal resistance of the plates. In figure 2, this corresponds to $e \longrightarrow 0$. This limit does not guarantee that the temperature of the plates – uniform though it might be in steady convection – will also remain constant at all times if the convection is unsteady. The existence of plumes indeed makes turbulent convection unsteady over a range of time and spatial scales. To ensure a constant and uniform plate temperature for every flow condition (i.e. every Rayleigh number) the plate should possess infinite thermal conductivity and heat capacity. Since every plate falls short of these ideal properties, the temperature uniformity can be realized only to within some degree of approximation since the surface temperature in experiments (figure 2*b*) is constant only on the *average* but not locally (in time or space). One should thus expect departures from the ideal case of numerical simulations (figure 2*a*). We shall argue that the departures are manifested through effects on plume generation.

As an aside, we should note that the effect of imperfectly conducting walls has been the subject of investigation near the onset of convection (e.g. Sparrow, Goldstein & Jonsson 1964; Busse & Riahi 1980), but we are unaware of comparable studies in the fully turbulent regime at high Rayleigh numbers.

In § 2, we describe numerical simulations in which the temperature boundary conditions of the lower plate are set for constant heat flux instead of constant temperature. The comparison in § 3 of the present results with those of previous simulations with constant-temperature boundary conditions (Verzicco & Camussi 2003; Verzicco 2003) shows that the differences between the two cases can account for most of the mismatch highlighted in figure 1(*a*). The simple dimensional argument

of §4 is intended to explain the altered plume dynamics and the difference in the computed Nusselt numbers. Section 5 provides some concluding remarks.

2. The problem and the numerical method

The buoyancy-driven flow developing in a cylindrical cell of aspect ratio 1/2 is analysed via direct numerical simulations of the Navier–Stokes equations with the Boussinesq approximation. The problem is similar to that addressed in Verzicco & Camussi (2003) and Amati *et al.* (2005), who analysed the configuration of figure 2(*a*) with $e=0$. The principal difference here is that the temperature boundary condition at the bottom plate is one of constant gradient rather than constant temperature. The configuration is shown in figure 2(*b*) with $e=0$, all surfaces being no-slip.

It must be stressed that the choice of constant heat flux was made only for the bottom plate because, in a real setup, the bottom plate is in contact with a heater while the top plate is usually connected to a thermostatic bath. Thus, the condition of constant heat flux may apply mostly to the lower plate. The thermocouple measurements of Cioni, Ciliberto & Sommeria (1997), made inside the plates, indeed found that the bottom plate approximated a constant-heat-flux surface while the top plate corresponded to constant-temperature boundary. The measurements of Cioni *et al.* were for mercury with copper plates, but similar circumstances prevail for other fluids at higher *Ra*. It is worth noting, however, that the condition of constant temperature holds only approximately also for the upper plate since a recirculating refrigerating fluid, for example, will have a temporally and spatially varying temperature within the top plate.

If $q=\partial\theta/\partial z|_w$ is the wall temperature gradient assigned at the bottom plate and h the height of the cell, temperature and velocity scales can be written, respectively, as qh and $\sqrt{g\alpha q h^2}$. The non-dimensional governing equations are then

$$\frac{\mathrm{D}\boldsymbol{v}}{\mathrm{D}t}=-\nabla p+\Theta\hat{\boldsymbol{z}}+\left(\frac{Pr}{Ra_q}\right)^{1/2}\nabla^2\boldsymbol{v},\qquad \nabla\cdot\boldsymbol{v}=0, \tag{2.1}$$

$$\frac{\mathrm{D}\Theta}{\mathrm{D}t}=\frac{1}{(PrRa_q)^{1/2}}\nabla^2\Theta, \tag{2.2}$$

with $\hat{\boldsymbol{z}}$ as the unit vector pointing opposite to gravity, $\boldsymbol{v}$ the velocity vector, p the pressure and Θ the non-dimensional temperature; $Ra_q=g\alpha q h^4/(\nu k)$ and $Pr=\nu/k$ are the Rayleigh and Prandtl numbers, respectively, with g denoting the acceleration due to gravity, α the isobaric thermal expansion coefficient, ν the kinematic viscosity and k the thermal diffusivity of the fluid.

The equations written in cylindrical coordinates are discretized on a staggered mesh by central second-order-accurate finite-difference approximations as described in Verzicco & Orlandi (1996). The resulting discretized system is solved by a fractional-step procedure with the elliptic equation inverted using trigonometric expansions in the azimuthal direction and the FISHPACK package (Swartzrauber 1974) for the other two directions. The time advancement of the solution is obtained by a hybrid low-storage third-order Runge–Kutta scheme. The numerical method is the same as that used by Verzicco & Camussi (2003) and Verzicco & Orlandi (1996), where further details and validation checks can be found.

Six main cases were run at Rayleigh numbers $Ra_q=2\times10^7$, 2×10^8, 2×10^9, 2×10^{10}, 2×10^{11} and 2.8×10^{13}, all with $Pr=0.7$. The numerical grids were $65\times49\times193$ for $2\times10^7\leqslant Ra_q\leqslant2\times10^9$ and $97\times49\times193$, $129\times97\times385$ and $193\times129\times513$

for the other three cases in the azimuthal, radial and vertical directions. The time integration of the equations was performed by an adaptive time step resulting in about 400 time steps for each large-eddy-turnover time at $Ra_q = 2 \times 10^7$, and in 1400 time steps at $Ra_q = 2.8 \times 10^{13}$. More details on the numerical technique and computational parameters can be found in Verzicco & Camussi (2003).

Note that, for the present problem, the temperature at the lower horizontal plate is constant only on the average and fluctuates in both time and space. If $\overline{\theta}_h$ is the mean lower plate temperature (for the upper plate it is assigned to be $\theta_c \equiv \overline{\theta}_c = 0$) the temperature difference of the setup is $\Delta = \overline{\theta}_h - \overline{\theta}_c$ and the Nusselt number is simply $Nu = qh/\Delta$. In order to compare the present results with those for constant temperature, we relate Ra_q with the usual Rayleigh number $Ra = g\alpha\Delta h^3/(\nu k)$ through $Ra = Ra_q \Delta/(qh) = Ra_q/Nu$, and scale velocity and temperature respectively with $\sqrt{g\alpha\Delta h}$ and Δ, thus yielding $\boldsymbol{u} = \boldsymbol{v}\sqrt{Nu}$ and $\theta = \Theta Nu$. This will allow the discussion of the flow dynamics for constant temperature and constant heat flux within a single framework.

2.1. *Grid refinement checks*

In Verzicco & Camussi (2003) and Amati *et al.* (2005), each of the flows at $Ra = 2 \times 10^7$ and $Ra = 2 \times 10^{11}$ were computed on two different grids in order to define the minimum resolution requirements for scaling up the simulations at higher Ra. Here, we perform the refinement check more systematically by selecting one representative flow condition and computing it on different meshes and time steps in order to quantify the effects of numerical resolution on the Nusselt number. For this purpose the flow at $Ra = 2 \times 10^{10}$ is a sensible choice on several counts. First, the Rayleigh number is already high enough for the Nusselt number of numerical simulations and experiments to be appreciably different, yet the mesh used in Verzicco & Camussi (2003) is coarse enough to allow further grid refinement in each direction. Further, in Amati *et al.* (2005), the flow at $Ra = 2 \times 10^{10}$ was the least resolved in space, so we may expect the resolution effects to be the largest.

The flow at $Ra = 2 \times 10^{10}$, which Verzicco & Camussi (2003) simulated on a grid $129 \times 97 \times 385$, in the azimuthal, radial and vertical directions, respectively, is recomputed now on grids $65 \times 49 \times 193$, $97 \times 65 \times 257$, $193 \times 129 \times 513$, $257 \times 193 \times 771$ and $385 \times 257 \times 1025$. For grids $193 \times 129 \times 513$ and $257 \times 193 \times 771$, the CFL stability parameter, which was set equal to 1.5 in the original simulation, has been halved. For the grid $385 \times 257 \times 1025$, the CFL has been further reduced to 0.25 for an even better refinement of the time step. The mesh of Verzicco & Camussi (2003) was 2.4 times larger than the Kolmogorov scale (η) in the bulk and had 6 nodes within the thermal boundary layer of thickness δ_θ with the first node at $\delta_\theta/10$. The two finest grids of the present study, $257 \times 193 \times 771$ and $385 \times 257 \times 1025$, correspond to 1.2η and 0.8η in the bulk, with 12 and 33 nodes within δ_θ and the first point at $\delta_\theta/18$ and $\delta_\theta/100$. The results in figure 3 show that, except for the coarsest case, all the computed Nusselt numbers are within the error bar of the original computation thus confirming that insufficient numerical resolution is not the cause of differences between simulations and experiments.

Furthermore, it should be stressed that all the simulations of Amati *et al.* (2005) for $2 \times 10^{11} \leqslant Ra \leqslant 2 \times 10^{14}$ had a resolution comparable to the refined cases of the present analysis. Therefore, for those simulations as well, all resolution effects should be expected to be within the error bars of the data of figure 3(*a*).

As a final check of the numerical code, we have repeated the computations of Shishkina & Wagner (2006) who used a grid of $193 \times 513 \times 111$ nodes in a $\Gamma = 10$

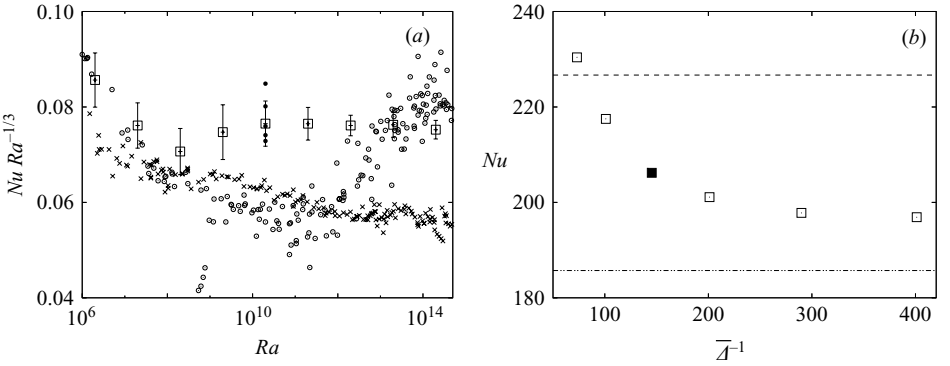

FIGURE 3. (*a*) Compensated Nusselt number versus Rayleigh number. Experimental data: ○, Chavanne *et al.* (2001); ×, Niemela *et al.* (2000). Numerical simulations: □, Amati *et al.* (2005); ●, present grid refinement data reported in detail in (*b*). (*b*) Nusselt number versus the inverse of the mean grid spacing at $Ra = 2 \times 10^{10}$. The symbol ■ is the value reported in (*a*) and the lines are the upper and lower bounds of the error bar.

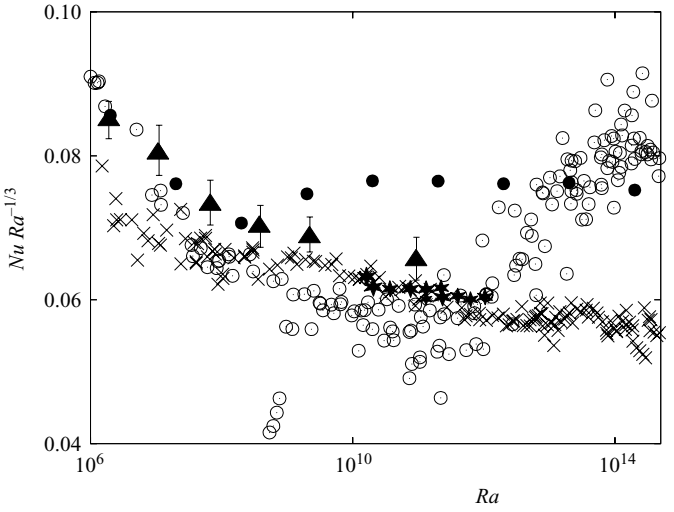

FIGURE 4. Compensated Nusselt number versus Rayleigh number. Numerical simulations: ●, Amati *et al.* (2005); ▲, present results with imposed heat flux on the lower horizontal plate. Experimental data: ○, Chavanne *et al.* (2001); ×, Niemela *et al.* (2000); ∗, Nikolaenko *et al.* (2005). Data for $\Gamma = 0.427$ and $\Gamma = 0.667$, both close to $1/2$, are taken from Nikolaenko *et al.* All other data are for $\Gamma = 1/2$.

cylindrical cell at $Pr = 0.7$ to simulate flows at $Ra = 10^5$, 10^6 and 10^7. For these Rayleigh numbers, their Nusselt numbers of 4.1, 8.2 and 16.4 compare well with our values 4.23 ± 0.18, 8.37 ± 0.22, 17.1 ± 0.43.

3. Results

An important quantitative result is the behaviour of the Nusselt number as function of the Rayleigh number for conditions of constant heat flux and constant temperature (see figure 4). The Nusselt numbers in the two cases are essentially the same up to about $Ra \approx 10^9$ but differ beyond. We also plot experimental data from Niemela

FIGURE 5. Results for the constant-heat-flux condition at the lower plate, $Ra_q = 2 \times 10^{11}$, ($Ra = 2.22 \times 10^9$) $Pr = 0.7$. (*a*) Instantaneous temperature distribution at the lower plate: thick ———, $\theta = \overline{\theta}_w$; blue, magenta and red, $\theta > \overline{\theta}_w$; yellow, green and cyan, $\theta < \overline{\theta}_w$. (*b*) Perspective view of the instantaneous temperature isosurface ($\theta = 0.8\overline{\theta}_w$) close to the lower plate. (*c*) Contour lines of vertical velocity at a distance of $\approx 0.015h$ from the lower plate; green and ———, positive velocities; red and ·····, negative velocities.

FIGURE 6. Results for constant-temperature boundary condition, $Ra = 2 \times 10^9$, $Pr = 0.7$. (*a*) instantaneous temperature gradient distribution at the lower plate: thick ———, $\partial\theta/\partial z|_w = Nu$; blue, red and yellow, $\partial\theta/\partial z|_w > Nu$; green and cyan, $\partial\theta/\partial z|_w < Nu$. (*b*) Perspective view of instantaneous temperature isosurface ($\theta = 0.8\overline{\theta}_w$) close to the lower plate. (*c*) Contour lines of vertical velocity at a distance of $\approx 0.015h$ from the lower plate; green and ———, positive velocities; red and ·····, negative velocities.

et al. (2000), Chavanne *et al.* (2001) and Nikolaenko *et al.* (2005). All the data are for closely similar geometries. They are close to the numerical data for the case of constant heat flux. An immediate suggestion from this is that the experimental boundary condition at the lower wall may be closer to the constant-heat-flux condition than to the constant-temperature condition. One should, however, be cautious. For instance, the constant-heat-flux boundary condition is applied directly to the fluid in simulations ($e = 0$ in figure 2*b*) while, in an experimental setup, a thick metal plate is interposed between the heater and the fluid ($e \neq 0$). This may account for the slightly larger Nu in numerical simulations, which cannot be ascribed to statistical uncertainty.

In order to understand the result, it is helpful to examine the flow dynamics associated with the two temperature boundary conditions. Figures 5 and 6 show instantaneous snapshots of the two flows close to the lower plate for the same Ra and Pr. In particular, for constant heat flux we show the wall temperature, a temperature isosurface and contours of vertical velocity (in figures 5*a*, 5*b* and 5*c*, respectively). The 'crests' in figure 5(*b*) show the formation of line plumes as confirmed by the positive (upward) vertical velocity at the same position. The wall temperature below each plume exceeds the average since the fluid, which is drained into the plumes from the sides, is essentially stagnant. This picture is reinforced by the observation that the wall temperature on both sides of the plumes is below the average and the vertical velocity is negative. The same behaviour for the surface temperature was reported by Hunt *et al.* (2003) for constant heat flux. On the other hand, when the wall temperature

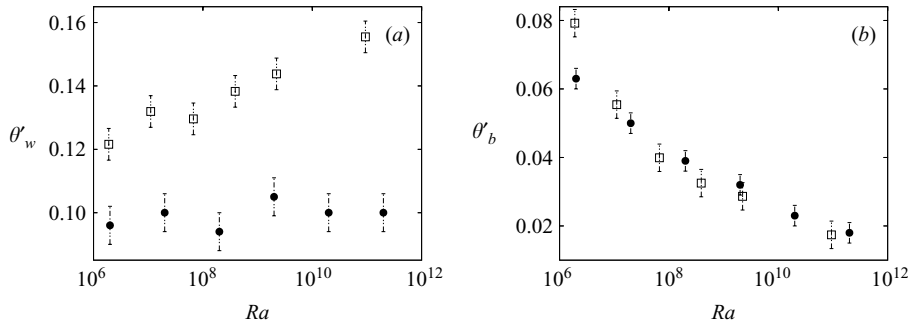

FIGURE 7. Comparison of temperature fluctuations at the wall and in the bulk as functions of the Rayleigh number for the constant-temperature (●) case and for the constant-heat-flux case. (□): (*a*) wall temperature r.m.s. (note that for the constant-heat-flux case it is evaluated at the wall while for the constant-temperature case it is taken to be the peak r.m.s. within the thermal boundary layer); (*b*) bulk temperature r.m.s.

is held constant, its gradient (figure 6*a*) can adjust to the demands of the local flow dynamics. Accordingly, on the sides of the plumes, the heat flux tends to rise above the average and the vertical velocity is again negative. The fundamental difference between the two flows is illustrated by the temperature isosurfaces (corresponding to 80% of the wall temperature). In fact, the flow in figure 6 can accommodate any heat flux by making the thermal boundary layer thinner without limit, while, in the flow in figure 5, a heat flux requirement that exceeds the boundary condition is met only by decreasing the wall temperature. This causes the plumes to be colder and less buoyant, so they carry less heat than in the constant-temperature case.

A quantitative view of the phenomena just described is given in figure 7(*a*, *b*) showing the wall and bulk temperature fluctuations for the two flows. The peak root-mean-square (r.m.s.) temperature within the thermal boundary layer is approximately constant for all *Ra* when the plate temperature is constant while, for the imposed heat flux case, the wall temperature fluctuations tend to increase with *Ra* and are larger than for constant temperature (figure 6*a*). The increased fluctuation level arises because, when the heat flux is prescribed, the temperature can fluctuate above and below the mean value of the plate $\overline{\theta}_c$. On the other hand, as shown in figure 6(*b*), the temperature fluctuations in the bulk are comparable in the two cases. This is so because only the hotter fluctuations at the bottom wall can produce thermal plumes, these being the source of fluctuations in the bulk. This finding can be interpreted with the help of figure 8, which shows that the velocity fluctuations in the bulk are smaller for constant heat flux than for constant temperature. The present findings on temperature fluctuations near the lower plate and in the bulk agree fully with Hunt *et al.* (2003) (see their figure 6), who found the fluctuation level to increase with *Ra* at the wall and to remain constant in the bulk. This suggests that, despite the large wall temperature fluctuations, only a part of them is due to plumes that are generally less intense for constant heat flux than for constant temperature. Since the power going into fluctuations is an increasing fraction of the thermal power input as the Rayleigh number increases (Niemela & Sreenivasan 2002), we should expect the differences between constant-heat-flux and constant-temperature flows to increase with *Ra*.

In the next section, we will show that if the boundary can provide the flow with any amount of heat flux, the heat carried by each plume is an increasing function of *Ra* while its temperature is a constant fraction of the temperature difference Δ. On

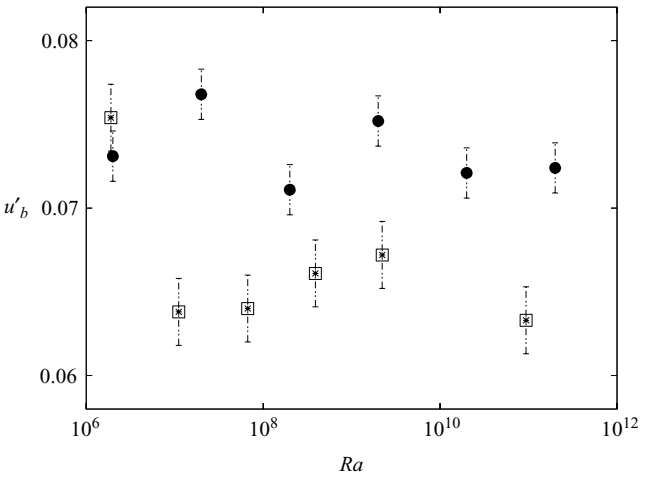

FIGURE 8. Comparison of velocity fluctuations in the bulk as a function of the Rayleigh number for constant-temperature (●) and constant-heat-flux (□) simulations.

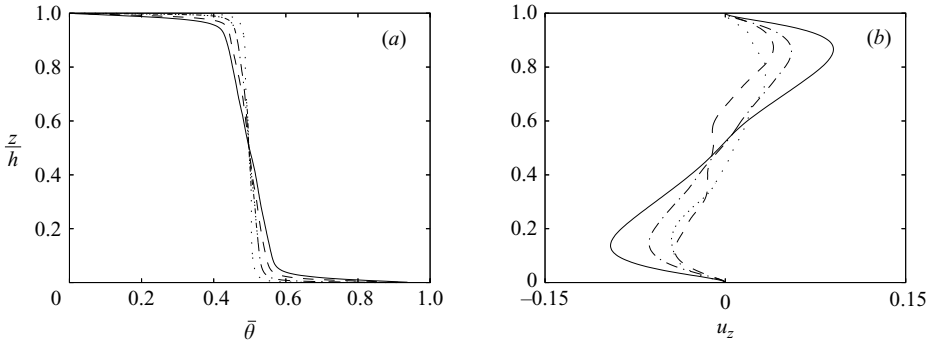

FIGURE 9. Averaged profiles of (*a*) temperature and (*b*) vertical velocity along the axis of the cell as functions of the Rayleigh number. ——, $Ra_q = 2 \times 10^8$; — — —, $Ra_q = 2 \times 10^9$; - - - -, $Ra_q = 2 \times 10^{11}$: ·····, $Ra_q = 2.8 \times 10^{13}$.

the other hand, if the heat flux is fixed, the plume temperature is a fraction of Δ that decreases with *Ra*. Figure 4 suggests, roughly, that the heat transport is affected when a threshold *Ra* is exceeded. Apart from these differences close to the lower plate, the flow with imposed heat flux is quite similar to that with constant temperature. The mean profiles along the axis of temperature and vertical velocity, shown in figure 9, are very close to those of Verzicco & Camussi (2003) (see their figure 13). So also are the vertical profiles of temperature r.m.s., with the obvious difference occurring near the lower and upper plates (figure 10). It is worth mentioning that Verzicco & Camussi (2003) estimated the thermal boundary layer thickness (δ_θ) from the position of the r.m.s. temperature peak as in the upper inset of figure 10. For the present problem this is possible only at the upper plate since for the lower boundary the peak of temperature r.m.s. is right at the wall (figure 10). We have therefore computed δ_θ for the lower wall following the procedure of Belmonte, Tilgner & Libchaber (1994), who linearly extrapolated the temperature profile from the wall until it reached the average temperature. The results for the two plates, reported in figure 11, show a similar behaviour.

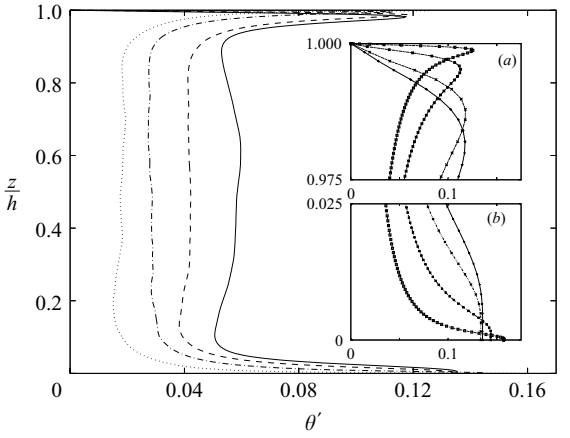

FIGURE 10. Averaged r.m.s. temperature profiles as function of the Rayleigh number. The insets are respectively enlargements of (*a*) the upper and (*b*) lower plates; the symbols indicate the position of the computational nodes. Lines as in figure 9.

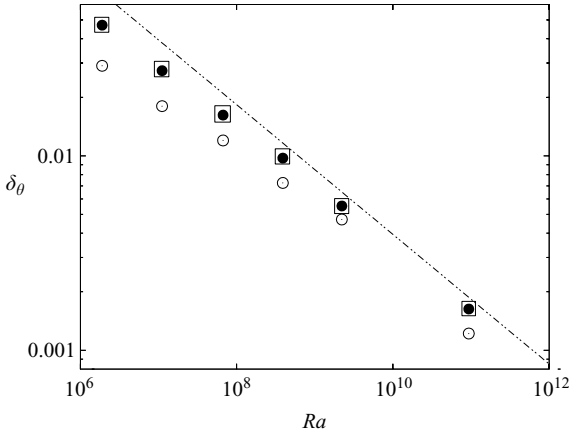

FIGURE 11. Thermal boundary layer thickness as a function of the Rayleigh number for the constant heat flux case: lower plate (●) and upper plate (□) for δ_θ computed from the linear extrapolation of the mean temperature profile. ○, δ_θ at the upper plate computed by the position of the peak in the r.m.s. value of the temperature fluctuation. The line follows the $-1/3$ power low.

4. A simple dimensional argument

We consider a simple dimensional argument in order to supplement the above discussion. In the case of constant temperature, the local wall temperature gradient $\partial\theta/\partial z|_w$ changes with space and time, and the heat transport through a surface element S is $Q_w = \lambda\langle\partial\theta/\partial z|_w\rangle S$, where λ is the thermal conductivity of the fluid and the angular brackets imply averaging of the gradient over time (also over space in view of homogeneity). Assume that a plume, generated in the area element S, leaves the plate with a vertical velocity u_z. If S is also the cross-section of the ascending plume, its heat flux can be estimated as $Q_p \approx \rho C_p \theta_p u_z S$, where ρ and C_p are the density and the specific heat at constant pressure, respectively, and $\theta_p = \Delta$ the temperature of the plume if it can be considered as a 'piece' of detached boundary layer (figure 12). This

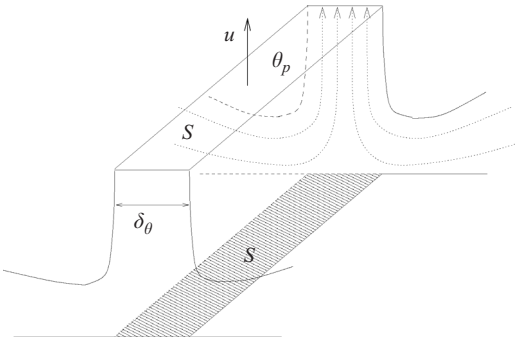

FIGURE 12. Schematic of a portion of thermal plume detaching from the lower plate.

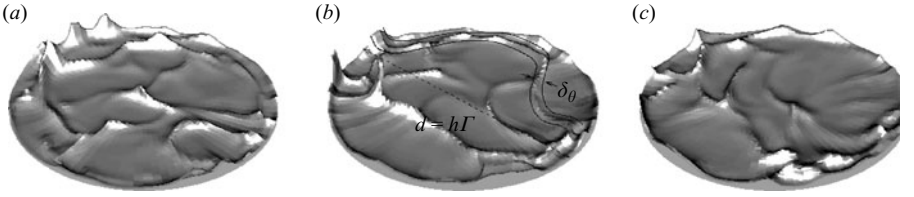

FIGURE 13. Perspective views of instantaneous temperature isosurfaces ($\theta = 0.8$) close to the lower plate. Simulation with constant temperature at the plate, $Ra = 2 \times 10^8$, $Pr = 0.7$: (*a*) $t = 185$, (*b*) $t = 190$ and (*c*) $t = 195$.

estimate for Q_p assumes that the plume receives the heat from a plate area S' which is the same as its cross-section S. In general, this will not be true since the heat is transported in and out of the plume also from the sides thus making S' bigger than S. It is reasonable to conjecture, however, that S' and S are proportional through a factor which, while different from unity, can be neglected in discussions of the scaling behaviour. According to flow visualizations and models (Theerthan & Arakeri 1998; Grossmann & Lohse 2004; Puthenveettil & Arakeri 2005) a typical plume is a two-dimensional sheet-like structure of thickness comparable to the thermal boundary layer δ_θ (line plume), which initially extends in the vertical direction, eventually to be bent by the mean wind (figure 13). Castaing *et al.* (1989) suggest that a plume accelerates up to a velocity for which buoyancy and viscous drag are in balance; for a two-dimensional sheet with lateral dimension comparable to the horizontal size of the cell, this vertical velocity can be estimated as $u_z \approx g\alpha\Delta\delta_\theta h\Gamma/\nu$, Γ being the aspect ratio of the cell.

If, as suggested by Castaing *et al.* (1989), a plume attains a velocity u_z such that buoyancy and drag are in equilibrium, we can write $\rho u_z^2 S' C_D/2 = \rho g\alpha\theta_p V$ where V and S' are, respectively, the volume and wet surface of the plume while θ_p is the plume temperature; we have $\theta_p = \Delta$ by considering a plume as a piece of detached thermal boundary layer. If the plume is mushroom-like, $S' \sim \delta_\theta H$ and $V \sim \delta_\theta^2 H$ while for a line plume $S' \sim LH$ and $V \sim \delta_\theta LH$; here $H \sim h$ is a vertical dimension of the plume and L a lateral coherence length. Finally, we assume that the plume is slow enough to consider the drag coefficient $C_D \sim 1/Re$ thus obtaining for the mushroom-like and line plumes $u_z \approx g\alpha\Delta\delta_\theta^2/\nu$ and $u_z \approx g\alpha\Delta\delta_\theta h\Gamma/\nu$ (corresponding to $Re = u_z\delta_\theta/\nu$ and $Re = u_z L/\nu$, after having neglected numerical coefficients of order one). The above derivation depends on the reference length chosen for the Reynolds number. In the Stokes regime we have assumed that this length must be representative of the plume 'wet' surface which results in a length L for the line plume and δ_θ for the mushroom

like plume. In contrast, if only the length δ_θ is used the rising velocity is identical in both cases and equal to that of Castaing *et al.* (1989). We wish to stress that the factor Γ in the velocity for the line plume arises from the assumption that the structure remains coherent over the whole width of the cell. This is realistic for configurations with $\Gamma \leqslant 1$ but unlikely for large aspect ratios; therefore, it should be intended as limited by unity. The other questionable hypothesis is $C_D \sim 1/Re$ since it implies very slow and purely viscous dynamics; for this reason, later in this section 4, the same arguments have been applied when considering that the plume attains the free-fall velocity or that the plume is driven by the convective heat flux.

With the above velocity estimate $u_z \approx g\alpha\Delta\delta_\theta h\Gamma/\nu$ and the definition $\delta_\theta \approx h/(2Nu)$ the ratio between plume flux Q_p and the local wall flux Q_w is

$$\frac{Q_p}{Q_w} \approx \frac{\rho C_p \Delta g\alpha \Delta \delta_\theta h\Gamma}{\lambda\langle\partial\theta/\partial z|_w\rangle\nu} \sim \frac{\Gamma Ra}{Nu^2}. \tag{4.1}$$

Once again we note that, while the neglected numerical factor in the last step of (4.1) might be different from unity, the scaling arguments are not altered and the conclusions remain valid.

The relation (4.1) shows that if $Nu \sim Ra^\beta$, with $\beta < 1/2$, the ratio between the heat drained by a plume and the average heat provided by the plate grows monotonically with Ra, suggesting that the boundary must cope with increasingly large localized heat flux spikes if the growth of the thermal plume is not to be saturated by an insufficient heat flux. It is important to note, however, that (4.1) relies on the assumption that a plume forms with enough heat (flux) to detach from the bottom plate at its temperature; this can only happen at every Rayleigh number for a boundary that has infinite heat capacity and maintains its temperature regardless of the required heat. This ideal system can be realized in a numerical simulation when the temperature is imposed as a boundary condition and the wall temperature gradient can attain any value demanded by the local flow dynamics (Amati *et al.* 2005). In a laboratory setup, on the other hand, the combination of a distributed heater, and a metal plate with good thermal conductivity (usually copper) acting as a 'heat reservoir', aims to approximate the constant-temperature condition. The plate has finite capacity and thermal conductivity, which makes the local wall temperature drop below the average if the required heat flux is too large for the thermal properties of the boundary. This suggests that in a real experimental apparatus the temperature boundary condition at the interface between the fluid and the plate can be a combination of constant temperature and constant heat flux, and their relative strengths depends on flow conditions.

For the case of fixed heat flux, since the line plume leaves the plate with an imposed heat flux, the ratio Q_p/Q_w remains constant (order one) and the previous relations can be used to determine the mean temperature of the plume, θ_p. An energy balance between the heat provided by the plate and that carried by the plume gives $u_z\theta_p = \lambda\langle\partial\theta/\partial z|_w\rangle/(\rho C_p)$, which, with the velocity $u_z \approx g\alpha\theta_p\delta_\theta h\Gamma/\nu$, yields

$$\theta_p \sim \Delta \frac{Nu}{Ra^{1/2}\Gamma^{1/2}}. \tag{4.2}$$

Once again, the correlation $Nu \sim Ra^\beta$ with $\beta < 1/2$ indicates that, as the Rayleigh number increases, the ratio θ_p/Δ decreases and produces colder plumes.

Note that the same argument essentially holds if we assume that a plume can accelerate up to a velocity comparable to the free-fall velocity (in reality, only a fraction of it is attained by the flow). In this case we have $u_z \approx (g\alpha\Delta h)^{1/2}$; with the

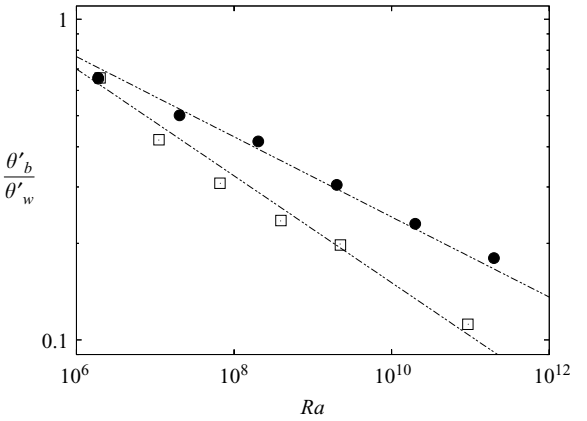

FIGURE 14. The r.m.s. temperature fluctuations in the bulk, normalized by the value at the wall, as a function of the Rayleigh number for constant temperature (●) and constant heat flux (□). For the former, the fluctuations are the peak value within the thermal boundary layer; for the latter, they are computed at the wall itself. Slopes of $-1/8$ and $-1/6$ are shown for comparison.

relations used for a plate at constant temperature one obtains $Q_p/Q_w \sim (Ra\,Pr)^{1/2}/Nu$. Once again, if $Nu \sim Ra^{\beta}$ with $\beta < 1/2$, as in (4.1), the ratio between the heat drained by a plume and the average heat provided by the plate grows monotonically with the Rayleigh number. On the other hand, if the plate can only provide a constant heat flux so that $Q_p/Q_w = O(1)$, we can compute the mean plume temperature, with the free-fall velocity as above, to be $\theta_p \sim \Delta[Nu^2/Ra\,Pr]^{1/3}$. This expression should be compared with (4.2); further, given the Nu dependence on Ra, the ratio θ_p/Δ decreases for increasing Ra, thus giving colder plumes.

The same conclusions are achieved also if we follow Hunt *et al.* (2003) who estimated the plume velocity as $u_z \approx (g\alpha F h)^{1/3}$, F being the convective heat flux, $F = \langle u'_z\theta' \rangle$. Since, for $Nu \gg 1$, we have $Nu \approx Fh/(k\Delta)$ we obtain $Q_p/Q_w \sim [Ra\,Pr/Nu^2]^{1/3}$; with $Nu \sim Ra^{\beta}$ and $\beta < 1/2$, this ratio grows monotonically with Ra. For a constant heat flux with $Q_p/Q_w \approx 1$, the mean plume temperature becomes $\theta_p \sim \Delta[Nu^2/Ra\,Pr]^{1/3}$, which, given the observed dependence of Nu on Ra, gives a decreasing θ_p/Δ for increasing Ra.

We wish to stress that relation (4.2) concerns only the plume temperature. It does not necessarily imply that the r.m.s. temperature at the wall (θ'_w) decreases with Ra as in figure 9(*a*). In fact, for increasing Rayleigh numbers, the flow becomes more turbulent and the mean wind more unsteady; since the wall temperature is not fixed, θ'_w tends to increase and remain larger than the peak r.m.s. of the imposed-temperature case. As already mentioned, despite the increased wall temperature fluctuations, the temperature r.m.s. in the bulk (θ'_b) is very similar to the constant-temperature case, perhaps even showing slightly smaller values. If we argue that, among all the wall temperature fluctuations, only those that are positively correlated with the vertical velocity are likely to reach the bulk, we can think of such events as indicating the plumes; thus, by examining the quantity θ'_b/θ'_w, one can track (in a statistical sense) how much of the produced temperature fluctuation has reached the bulk through plume dynamics. The results for constant temperature and constant heat flux are given in figure 14. They show that, consistent with (4.2), a more rapid decrease with Ra occurs for the constant-heat-flux case while the fluctuations in the constant

temperature conditions follow the $-1/8$ (or $-1/7$) power law, as already observed in experiments (Wu 1991; Niemela *et al.* 2000). Although it might be coincidental, the scenario just conjectured is reinforced by the observation that, if we insert the correlation $Nu \sim Ra^{1/3}$ in (4.2), we obtain $\theta_p \sim \Delta Ra^{-1/6}$ – this being the slope observed in figure 14.

5. Concluding remarks

In the present study we have considered the differences produced in thermal convection for the cases of constant-heat-flux boundary and constant-temperature boundary. The results indicate that for $Ra < 10^9$ the two cases are comparable while, for higher Rayleigh numbers, the constant-heat-flux case yields lower Nusselt number. The reason appears to be that the growth of the thermal plumes with constant heat flux is inhibited by the decrease of the wall temperature. This reduction is comparable to the amount by which experimental data fall below the simulations. Even so, it does not necessarily follow that the laboratory setups have a constant-heat-flux boundary condition at the lower plate. In fact, in a real setup, a thick metal plate with good thermal conductivity is interposed between the heater and the fluid, which tends to homogenize the temperature at the plate-fluid interface and acts as a heat reservoir. It is worth repeating that, in order to ensure a constant and uniform plate temperature for every flow condition (every Rayleigh number), the plate should have infinite thermal conductivity and heat capacity. In practice, every plate has finite thermal properties, and the temperature uniformity can be realized only with some degree of approximation.

A detailed analysis of the coupling between flow conditions and plate thermal properties has been performed by Chillá *et al.* (2004) who have shown that any plate produces temperature fluctuations that interfere with the heat transport for large enough *Ra*. A good plate should have a thermal conductivity (λ_p) much larger than that of the fluid so that the temperature distribution on the plate remains uniform. However, the *effective* thermal conductivity of the fluid $\lambda_f Nu$ could eventually become comparable to λ_p for very high *Ra*. At this condition the temperature uniformity can still be maintained if the specific heat capacity of the plate ($\rho_w C_w$) is much larger than that of the fluid (ρC_p). According to Chillá *et al.* (2005), the specific heat capacities govern the temperature fluctuations through the ratio $[\rho_w C_w/(\rho C_p)]^{0.5}$. For the experiments of Niemela *et al.* (2001) and Chavanne *et al.* (2001), which used cryogenic helium and oxygen-free copper, $[\rho_w C_w/(\rho C_p)]^{0.5} \simeq 0.5$. This quantity for Nikolaenko *et al.* (2005), who used water and copper, is 0.9. Since the two values are not farapart, it is not surprising that the results in figure 4 are similar. The experiments with pressurized gasses are better by an order of magnitude. Fleischer & Goldstein (2002) used argon and nitrogen and for their conditions $5.9 \leqslant [\rho_w C_w/(\rho C_p)]^{0.5} \leqslant 7$. For pressurized SF_6 in the experiments by Ashkenazi & Steinberg (1999) $2.2 \leqslant [\rho_w C_w/(\rho C_p)]^{0.5} \leqslant 5.4$; in these studies there is the additional complication of the Prandtl number and cell aspect ratio variation – even though the Nusselt number measurements are in rough agreement with results from water and cryogenic-gas experiments.

A good way to confirm the findings of the present paper is to conduct experiments at high Rayleigh numbers using an ambient temperature gas and copper plates; for example, for air and copper, $[\rho_w C_w/(\rho C_p)]^{0.5} \simeq 53$, which is much larger than that in existing experiments. Unfortunately, air at ambient temperature requires very large setups (large values of h) if the increase in *Ra* is to be attained without sacrificing the

Boussinesq approximation. The largest tank operating with air at present is 'the barrel of Ilmeneau', where the top cooling plate is made of aluminium while the bottom hot plate is a 5 cm thick concrete layer (Du Puits *et al.* 2007). According to the authors, owing to the relatively small heat diffusivity of the concrete, the boundary condition of the heating plate is of nearly constant heat flux. Their setup is thus nominally similar to the present numerical arrangement and their heat transfer data show good agreement with the present findings. This agreement, however, should be taken with caution on several counts. The aspect ratio of 'the barrel of Ilmeneau' varies from $\Gamma = 1.13$ up to $\Gamma = 11.3$ and, as noted by the authors, their data in the high end of the Ra range might be subject to non-Boussinesq effects. In addition, the heat flux through the sidewall is countered by an active heating system and the heat radiation between the horizontal plates is taken into account by a model while the heat losses to the ground are estimated by a single-point measurement (Du Puits *et al.* 2007).

A better verification of the present findings might be possible if 'the barrel of Ilmeneau' is provided with a better heating plate, changing the situation to a constant-temperature boundary condition within 1 K (R. Du Puits, private communication). Another interesting possibility, already attempted by J. J. Niemela (private communication), is as follows. The lower plate was fabricated from oxygen-free copper 'sponge' of about 60% porosity with nearly micron-sized pores. The plate retained the same high value of thermal conductivity as copper, but its heat capacity increased by several orders of magnitude because of the entrained fluid – thus providing an effectively constant-temperature boundary condition (high values of thermal conductivity and heat capacity). These unpublished experiments were designed to test the effect of boundary condition on the onset of convection. They detected no measurable difference (unlike the calculations of Sparrow *et al.* 1964), but no heat transport measurements at high Ra have been made with this arrangement.

We thank Dr Joe Niemela for several useful discussions. The simulation for constant temperature conditions were performed at the computing centre CASPUR and the assistance of Drs F. Massaioli and G. Amati is gratefully acknowledged. Part of the simulations for constant heat flux were made at the computing centre CINECA with a grant account, for which we thank Dr G. Erbacci.

REFERENCES

Ahlers, G. 2001 Effect of sidewall conductance on heat-transport measurements for turbulent Rayleigh-Benard convection. *Phys. Rev.* E **63**, 015303.

Ahlers, G., Araujo, F. F., Funfshilling, D., Grossmann, S. & Lohse, D. 2007 Non-Oberbeck-Boussinesq Effects in Gaseous Rayleigh-Bnard Convection *Phys. Rev. Lett.* **98**, 054501.

Ahlers, G. & Xu, X. 2001 Prandtl number dependence of heat transport in turbulent Rayleigh–Bénard convection *Phys. Rev. Lett.* **86**, 3320–3323.

Amati, G., Koal, K., Massaioli, F., Sreenivasan, K. R. & Verzicco, R. 2005 High-Rayleigh number turbulent thermal convection under strictly Boussinesq approximation. *Phys. Fluids* **17**, 121701.

Ashkenazi, S. & Steinberg, V. 1999 High Rayleigh number turbulent convection in a gas near the gas–liquid critical point. *Phys. Rev. Lett.* **83**, 3641–3644.

Belmonte, A., Tilgner, A. & Libchaber, A. 1994 Temperature and velocity boundary layers in turbulent convection *Phys. Rev.* E **50**, 269–279.

Brown, E., Nikolaenko, A., Funfschilling, D. & Ahlers, G. 2005 Heat transprt in turbulent Rayleigh-Benard convection: Effect of finite top- and bottom-plate conductivity. *Phys. Fluids* **17**, 075108.

Busse, F. H. & Riahi, N. 1980 Nonlinear convection in a layer with nearly insulating boundaries. *J. Fluid Mech.* **96**, 243–256.

Castaing, B., Gunaratne, G., Heslot, F., Kadanoff., L., Libchaber, A., Thomae, S., Wu, X. Z., Zaleski, S. & Zanetti, G. 1989 Scaling of hard thermal turbulence in Rayleigh-Bénard convection. *J. Fluid Mech.* **204**, 1–30.

Chaumat, S., Castaing, B. & Chillá, F. 2002 Rayleigh-Bénard cells: influence of the plate properties *Advances in Turbulence IX*, *Proc. 9th Euro. Turb. Conf.* (ed. I. P. Castro & P. E. Hancock.) CIMNe, Barcelona 2002, id:46,1.

Chavanne, X., Chillá, F., Chabaud, B., Castaing, B. & Hebral, B. 2001 Turbulent Rayleigh-Bénard convection in gaseous and liquid He. *Phys. Fluids* **13**, 1300–1320.

Chillá, F., Rastello, M., Chaumat, S. & Castaing, B. 2004 Ultimate regime in Rayleigh-Bénard convection: The role of plates. *Phys. Fluids* **16**, 2452–2456.

Cioni, S., Ciliberto, S. & Sommeria, J. 1997 Strongly turbulent Rayleigh-Bénard convection in mercury: comparison with results at moderate Prandtl number. *J. Fluid Mech.* **335**, 111–140.

Du Puits, R., Resagk, C., Tilgner, A., Busse, F. H. & Thess, A. 2007 Structure of thermal boundary layers in turbulent RayleighBénard convection. *J. Fluid Mech.* **572**, 231–254.

Fleisher, A. S. & Goldstein, R. J. 2002 High Rayleigh number convection of pressurized gases in a horizontal enclosure. *J. Fluid Mech.* **469**, 1–12.

Grossmann, S. & Lohse, D. 2001 Thermal convection for large Prandtl numbers. *Phys. Rev. Lett.* **86**, 3316–3319.

Grossmann, S. & Lohse, D. 2004 Fluctuations in turbulent Rayleigh-Bénard convection. *Phys. Fluids* **16**, 4462–4472.

Hunt, J. C. R., Vrieling, A. J., Nieuwstadt, F. T. M. & Fernando, H. J. S. 2003 The influence of the thermal diffusivity of the lower boundary on eddy motion in convection. *J. Fluid Mech.* **491**, 183–205.

Malkus, M. V. R. 1954 Heat transport and spectrum of thermal turbulence. *Proc. R. Soc. Lond.* A **225**, 196.

Niemela, J. J., Skrbek, L., Sreenivasan, K. R. & Donnelly, R. J. 2000 Turbulent convection at very high Rayleigh numbers. *Nature* **404**, 837–840.

Niemela, J. J., Skrbek, L., Sreenivasan, K. R. & Donnelly, R. J. 2001 The wind in confined thermal convection. *J. Fluid Mech.* **449**, 169–178.

Niemela, J. J. & Sreenivasan, K. R. 2002 Thermal fluctuations and their ordering in turbulent convection. *Physica* A **315**, 203–214.

Niemela, J. J. & Sreenivasan, K. R. 2003 Confined turbulent convection. *J. Fluid Mech.* **481**, 355–384.

Niemela, J. J. & Sreenivasan, K. R. 2006 Turbulent convection at high Rayleigh numbers and aspect ratio 4. *J. Fluid Mech.* **481**, 355–384.

Nikolaenko, A., Brown, E., Funfschilling, D. & Ahlers, G. 2005 Heat transport by turbulent Rayleigh-Benard convection in cylindrical cells with aspect ratio one and less. *J. Fluid Mech.* **523**, 251–260.

Puthenveettil, B. A. & Arakeri, J. H. 2005 Plume structure in high-Rayleigh-number convection. *J. Fluid Mech.* **542**, 217–249.

Roche, P. E., Castaing, B., Chabaud, B., Hébral, B. & Sommeria, J. 2001 Side wall effects in Rayleigh-Bénard experiments. *Euro. Phys. J.* B **24**, 405–408.

Roche, P. E., Castaing, B., Chabaud, B. & Hebral, B. 2002 Prandtl and Rayleigh numbers dependences in Rayleigh–Bénard convection. *Europhys. Lett.* E **58**, 693–698.

Shishkina, O. & Wagner, C. 2006 Analysis of thermal dissipation rates in turbulent Rayleigh-Bénard convection. *J. Fluid Mech.* **546**, 51–60.

Shraiman, B. I. & Siggia, E. D. 1990 Heat transport in high Rayleigh number convection. *Phys. Rev.* A **42**, 3650–3653.

Sparrow, E. M., Goldstein, R. J. & Jonsson, V. K. 1964 Thermal instability in a horizontal fluid layer: effect of boundary conditions and non-linear temperature profile. *J. Fluid Mech.* **20**, 35–46.

Stringano, G. & Verzicco, R. 2006 Mean flow structure in thermal convection in a cylindrical cell of aspect ratio one half. *J. Fluid Mech.* **548**, 1–16.

Swartzrauber, P. N. 1974 A direct method for the discrete solution of separable elliptic equations. *SIAM J. Numer. Anal.* **11**, 1136–1150.

Theerthan, A. S. & Arakeri, J. H. 1998 A model for near-wall dynamics in turbulent Rayleigh-Bénard convection. *J. Fluid Mech.* **373**, 221–254.

Verzicco, R. 2002 Side wall finite conductivity effects in confined turbulent thermal convection. *J. Fluid Mech.* **473**, 201–210.

Verzicco R. 2003 Turbulent thermal convection in a closed domain: viscous boundary layer and mean flow effects *Euro. Phys. J.* B **35**, 133–141.

Verzicco, R. 2004 Effect of non-perfect thermal sources in turbulent thermal convection. *Phys. Fluids* **16**, 1965–1979.

Verzicco, R. & Camussi, R. 2003 Numerical experiments on strongly turbulent thermal convection in a slender cylindrical cell. *J. Fluid Mech.* **477**, 19–49.

Verzicco, R. & Orlandi, P. 1996 A finite-difference scheme for three-dimensional incompressible flow in cylindrical coordinates. *J. Comput. Phys.* **123**, 402–414.

Wu, X.-Z. 1991 Along a road to developed turbulence: free thermal convection in low temperature helium gas. PhD thesis, University of Chicago.

Xia, K. Q., Lam, S. & Zhou, S. Q. 2002 Heat-Flux measurement in high-Prandtl-number turbulent Rayleigh-Bénard convection. *Phys. Rev. Lett.* **88**, 064501-1–4.